EDGE ARTICLE

Check for updates

Debut of enzyme-responsive anionic cyanine for overlap-free NIR-II-to-I dual-channel tumour imaging†

Feiyi Chu,[a] Bin Feng,[a] Yiyang Zhou,[a] Min Liu, [ID][ab] Hailiang Zhang,[a] Meihui Liu,[a] Qian Chen,[c] Shengwang Zhang,[c] Yeshuo Ma,[c] Jie Dong, [ID][a] Fei Chen [ID][a] and Wenbin Zeng [ID] *[a]

Bridging the disparity between traditional surgical resection imaging and *ex vivo* histopathology, fluorescence imaging is considered a promising tool in disease diagnosis and imaging navigation. Nevertheless, its usefulness is undermined by the variability of single-wavelength fluorescence signals and limited penetration of NIR-I (650–900 nm) bioimaging. In this work, we present a novel NIR-II ratiometric fluorescent probe (**CFC-GSH**) with γ-glutamyl transpeptidase (GGT) sensitivity for multifunctional bioimaging. This probe leverages a GSH-capped anionic cyanine, with advantages of high brightness, excellent photostability, high specificity and favourable biocompatibility. **CFC-GSH** exhibits an intrinsically stable NIR-II signal prior to triggering, which can be utilized for *in vivo* systemic circulation vessel outlining and microvascular imaging. At the tumour site with GGT over expression, an intramolecular S,N-rearrangement would initiate the conversion of sulphur-substituted cyanine to amino-substituted cyanine, resulting in a significant emission shift of 270 nm. Using the dual-channel signal changes, **CFC-GSH** effectively differentiates between subcutaneous hepatocellular carcinoma (HCC) and normal tissue and precisely localizes metastatic HCC tumours in the abdominal cavity. These results reveal that **CFC-GSH** exhibits promising potential as a multiprospective candidate tool for fluorescence screening and diagnostic imaging in various biological scenarios.

Introduction

The limitations of conventional *in vivo* imaging techniques, particularly in spatial resolution and tissue penetration depth, have driven the exploration of novel methods with superior bioimaging performance.[1–4] The second near-infrared (NIR-II) window has garnered significant attention due to its superior attributes, including enhanced deep tissue penetration, high resolution, and minimal tissue autofluorescence and photodamage.[5–8] However, traditional probes suffer from inherent background signals, hindering accurate target detection.[9–11] Activatable probes have emerged as a solution in the visible and NIR-I regions, but designing activatable NIR-II probes remains challenging.[12,13] This is primarily due to the lack of generalizable chemical strategies for modulating NIR-II emission, especially in the development of enzyme-activated

probes with high catalytic efficiency and substrate selectivity.[14,15]

Gamma (γ)-glutamyl transpeptidase (GGT), a key enzyme in glutathione metabolism primarily found in the liver, is upregulated in a variety of tumours and plays a vital role in their genesis, invasion, and metastasis.[16–19] Therefore, GGT is considered an important biomarker of tumours, and quantitatively detecting dynamic GGT activity is clinically significant for early diagnosis, accurate pathologic staging, intraoperative navigation and efficacy assessment of tumours.[19–22] Conventional GGT detection techniques, such as *p*-nitroaniline-based colorimetric analysis, electrochemistry, and high-performance liquid chromatography (HPLC), suffer from inherent drawbacks, such as intricate procedural requirements and complicated sample processing (Table S1†).[1,23–26] These factors pose a great challenge in obtaining real-time GGT levels in the organism. In contrast, optical imaging methods, especially probes working in the near-infrared (NIR) window (Table S2†), offer convenient and noninvasive methods for visualizing GGT in organisms due to their ability to provide *in situ* and real-time information.[27–33] Nevertheless, most NIR probes rely on fluorescence signals emitted at a single wavelength, which can be affected by the probe concentration, instrument parameters, and the dynamic biological environment.[1,34–37] In addition, the

[a]Xiangya School of Pharmaceutical Sciences, Central South University, Changsha, 410078, PR China. E-mail: wbzeng@hotmail.com

[b]Department of Pharmacy, Xiangya Hospital, Changsha 410008, PR China

[c]Third Xiangya Hospital, Central South University, Changsha 410013, PR China

† Electronic supplementary information (ESI) available. See DOI: https://doi.org/10.1039/d4sc06459c

conventional strategy for developing GGT-activatable probes involves linking a γ-glutamyl group to the fluorophore *via* an amide bond.[29–32,38–40] In this context, steric hindrance from the fluorophore near the enzymatic cleavage site may reduce the probe's affinity for the enzyme.[27,39] Moreover, enzymatic cleavage of the γ-glutamyl bond releases the fluorophore with an unprotected amine group, making it susceptible to potential oxidation or acylation by other enzymes in the biological system, leading to a complicated fluorescence response.[41,42] Thus, developing NIR ratiometric fluorescent probes with optimized kinetic profiles and stable signal output for GGT detection remains a challenge.

In this work, we constructed a novel NIR ratiometric probe, **CFC-GSH**, by directly conjugating GSH, a natural substrate of GGT, to a tricyanofuran (TCF)-ended anionic cyanine (Scheme 1). Upon enzymatic cleavage of the γ-glutamyl bond, the released amino group in the cysteinyl-glycine residue undergoes intramolecular cascade cyclization, yielding amino-substituted cyanine and resulting in a remarkable emission shift from 930 nm to 660 nm. Additionally, the rearranged amino-substituted product does not contain a free amine group, thus eliminating the possibility of amines being oxidized or acylated by other enzymes. Compared to reported GSH-based probes, polymethine-derived **CFC-GSH** exhibits an unprecedented shift from NIR-II to NIR-I fluorescence, with zero overlap in the emission spectra. The deep tissue penetration capability of NIR fluorescence enables the diagnosis and monitoring of subcutaneous tumours and metastasized tumours in the abdominal cavity of HCC through dual-channel imaging of GGT activities in a mouse model. To the best of our knowledge, **CFC-GSH** is the first ratiometric probe using NIR-II (900–1700 nm) signals to track GGT activities *in vivo*.

Results and discussion

Probe design and synthesis

Fluorescence imaging in the near-infrared II (NIR-II, 900–1700 nm) window provides deeper tissue penetration and higher resolution than NIR-I because it further minimizes tissue autofluorescence, absorption, and scattering.[5–7,43] To obtain a NIR-II probe with GGT-triggerable fluorescence, GSH is chosen as the enzymatic substrate and conjugated to an anionic cyanine scaffold featuring tricyanofuran ends to afford the probe **CFC-GSH**. Anionic cyanine exhibits significantly red-shifted photophysical properties compared to its cationic analogy, and particularly the tricyanofuran-terminated polymethine exhibits NIR-II fluorescence with high photostability.[44–47] Prior to GGT incubation, **CFC-GSH** is expected with inherent NIR-II signals due to the large π-conjugated system in the heptamethine chromophore.[44] As shown in Fig. 1, upon enzymatic cleavage of the γ-glutamyl bond, the amino group released in the cysteinyl-glycine residue promotes an intramolecular cascade arrangement of thiolate, which proceeds through a five-membered cyclic transition state to produce amino-substituted **CFC-NCS**. Given the unique cascade arrangement,[38,48] a significant bathochromic shift in absorption and fluorescence would be observed, promising the detection of GGT in a ratiometric mode in the NIR window. Of note, there is no free amine group in **CFC-NCS**, thus eliminating the interference from oxidation or acylation from other enzymes in the biological environment.

The probe **CFC-GSH** was conveniently synthesized from the nucleophilic substitution of the free thiol group of GSH with chlorine on anionic polymethine scaffold **CFC-Cl**, as presented in Scheme S1.† **CFC-GSH** and **CFC-Cl** were characterized by ^{1}H NMR, ^{13}C NMR and HRMS, respectively (Fig. S1–S5†).
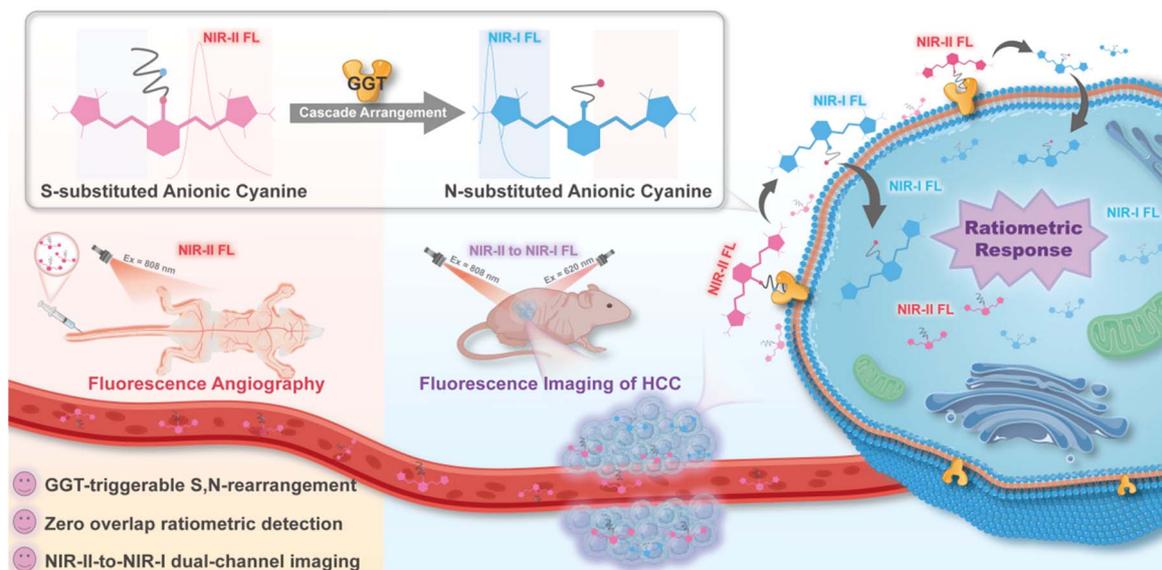
Scheme 1 Schematic diagram of NIR-II transpeptidase-triggered fluorescent probe **CFC-GSH** for multifunctional bioimaging. The anionic cyanine conjugate **CFC-GSH** exhibited an intrinsic NIR-II signal prior to activation by transpeptidases, which can be used for fluorescence angiography of systemically circulating vascular profiles. At the tumour site, the probe exhibited an unprecedented emission shift from NIR-II to NIR-I, enabling accurate hepatocellular carcinoma (HCC) surveillance.
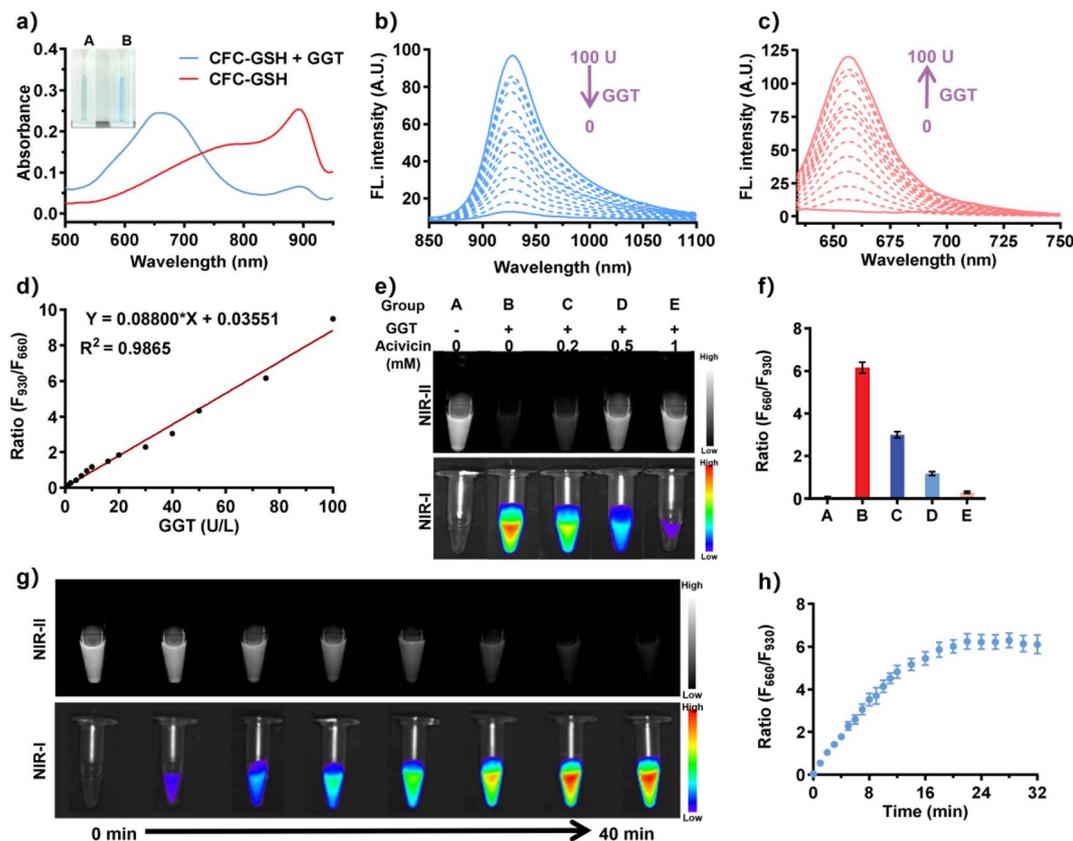
Fig. 1 (a) Absorption spectra of **CFC-GSH** (5 μM) in the absence (A) and presence (B) of GGT (100 U per L). (b) NIR-II (λ_{ex} = 808 nm) and (c) NIR-I (λ_{ex} = 620 nm) fluorescence spectra of **CFC-GSH** (5 μM) in the presence of different concentrations of GGT (0–100 U per L) for 30 min. (d) The linear relationship between the fluorescence intensity ratio (F_{660}/F_{930}) of **CFC-GSH** (5 μM) and GGT activity (0–100 U per L). (e) NIR-II (upper panel, λ_{ex} = 808 nm) and NIR-I (lower panel, λ_{ex} = 605 nm) fluorescent images of **CFC-GSH** (5 μM) to (A) PBS, (B) GGT (80 U per L), (C) GGT (80 U per L) + acivicin (0.2 mM), (D) GGT (80 U per L) + acivicin (0.5 mM), and (E) GGT (80 U per L) + acivicin (1 mM). (f) Fluorescence intensity ratio (F_{660}/F_{930}) of the groups in (e). (g) Time-dependent NIR-II (upper panel, λ_{ex} = 808 nm) and NIR-I (lower panel, λ_{ex} = 605 nm) fluorescent images of **CFC-GSH** (5 μM) in the presence of GGT (80 U per L) at different times (0–40 min). (h) Kinetic time curve for the fluorescence intensity ratio (F_{660}/F_{930}) of **CFC-GSH** (5 μM) incubated with GGT (80 U per L). Data are presented as mean ± s.d. (n = 3).

Spectral response to GGT

To evaluate the capability of GGT activation, the UV/vis absorption spectra of **CFC-GSH** in the absence and presence of GGT were evaluated in phosphate-buffered saline (PBS) solution. As shown in Fig. 1a, upon incubation with GGT, the absorption bands of **CFC-GSH** at 890 nm decreased gradually, whereas a new absorption peak emerged at 650 nm concomitantly. Along with the bathochromic shift of *ca.* 240 nm in the absorption spectra, a distinct colour change from green to blue was observed (Fig. 1a, inset). Next, the fluorescence titration experiments of **CFC-GSH** were carried out. In the absence of GGT, **CFC-GSH** exhibited fluorescence in the NIR-II region with a peak at 930 nm (λ_{ex} = 808 nm), which could be attributed to the large π-conjugated system existing in the tricyanofuran-ended heptamethine chromophore. After incubation with GGT, the initial NIR-II fluorescence decreased in a dose-dependent behaviour, whereas new fluorescence increased gradually at 660 nm (λ_{ex} = 620 nm) (Fig. 1b and c). The remarkable bathochromic shift (*ca.* 270 nm) in the fluorescent signal from NIR-II to NIR-I confirms the enzymatic cleavage of γ-glutamyl linkage in **CFC-GSH**. To our delight, zero overlap was

found in the two fluorescence spectra, which is beneficial for highly sensitive detection of GGT activity in potent ratiometric mode with self-calibration characteristics.[49,50] Harnessing the fluorescence intensity ratio (F_{660}/F_{930}) changes, the NIR ratiometric detection of GGT can be established with **CFC-GSH**. As shown in Fig. 1d, the fluorescence intensity ratio (F_{660}/F_{930}) exhibited a satisfactory linear relationship with the GGT concentration at 1–100 U per L (R^2 = 0.9865). The limit of detection (LOD) was determined to be 0.04 U per L ($3\sigma/k$), which meets the requirement for GGT detection in biological samples with the desired sensitivity. In contrast, the fluctuations of fluorescence signals appeared to be blocked when the working system was pretreated with glutamine analogues acivicin, an inhibitor of GGT[51] (Fig. 1e). Moreover, the fluorescence intensity ratio (F_{660}/F_{930}) decreased in an acivicin dose-dependent behaviour, demonstrating that GGT is essential for triggering optical changes (Fig. 1f and S6†).

Sensing mechanism

To investigate the responsive mechanism, we first explored the binding mode of **CFC-GSH** to GGT using molecular docking
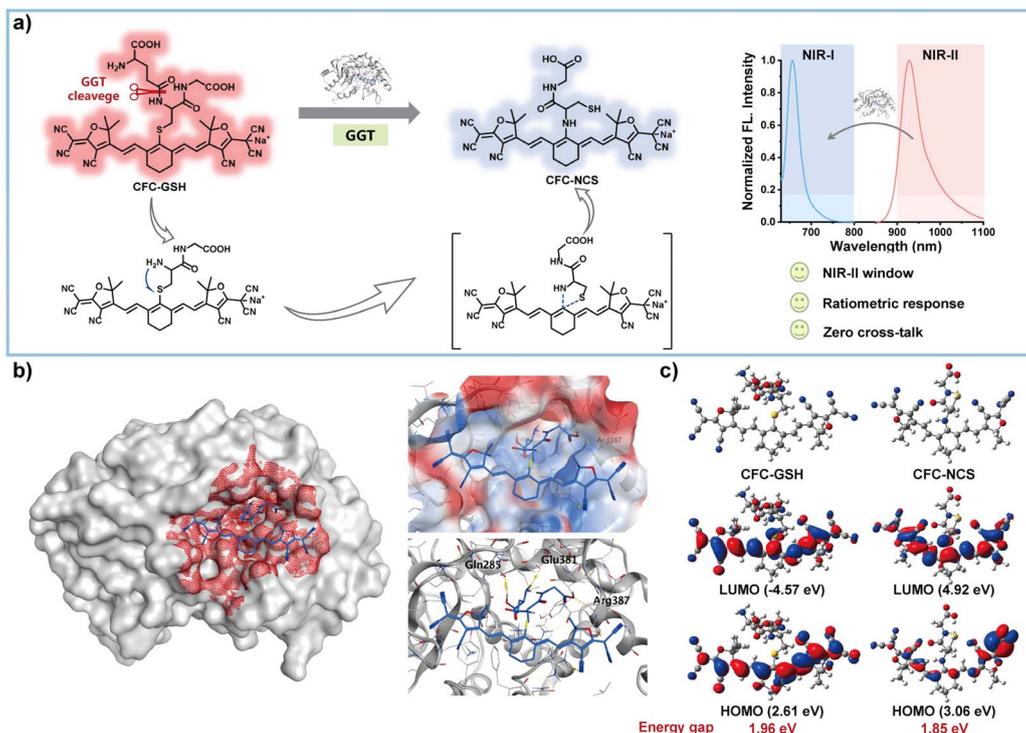
Fig. 2 (a) Schematic illustration of the sensing mechanism of **CFC-GSH** for GGT. (b) Molecular docking simulation of the binding mode of **CFC-GSH** to the catalytic pocket of GGT. (c) Frontier molecular orbital of probe **CFC-GSH** and amino-substituted product **CFC-NCS**.

simulations.[2,52] As shown in Fig. 2b, the recognition group γ-glutamyl unit can enter the enzymatic pocket successfully and form hydrogen bonds with the surrounding amino acid residues (Gln 285, Glu 381 and Arg 387), suggesting the high affinity of GSH-derived **CFC-GSH** to GGT. In addition, the fluorophore anionic polymethine was stuck outside the pocket, which may be attributed to the cysteine residue in GSH that could separate the cleavage site away from the cyanine scaffold, thereby diminishing the steric effect from the fluorophore. To validate the subsequent enzymatic activation, high-performance liquid chromatography (HPLC) analysis was carried out, as shown in Fig S7.† After incubation with GGT, the peak corresponding to **CFC-GSH** (3.11 min) decreased while another peak emerged at 5.17 min, which was further dominated as the incubation time prolonged (10.0 min). The generation of amino-substituted **CFC-NCS** was identified by the HRMS analysis (Fig. S8†). The incubation of **CFC-GSH** with GGT manifested a mass peak at 675.2106 identical to that of **CFC-NCS** (m/z: calc., 675.2143). These results supported that the enzymatic hydrolysis of the γ-glutamyl bond in **CFC-GSH** underwent a subsequent intra-molecular rearrangement cascade reaction to produce amino-substituted polymethine.[53,54] To rationalize the spectral change in the presence of GGT, the frontier molecular orbital of probe **CFC-GSH** and amino-substituted product **CFC-NCS** were calculated using Gaussian 16.[55,56] As shown in Fig. 2c, both the highest occupied molecular orbital (HOMO) and lowest unoccupied molecular orbital (LUMO) of **CFC-GSH** are located mainly in the heptamethine scaffold, while there is partial redistribution of the electronic density on the HOMO and

LUMO of **CFC-NCS**. The energy gap of **CFC-GSH** (1.96 eV) is larger than that of **CFC-GSH** (1.86 eV), which could rationalize the bathochromic shift of absorption wavelengths of **CFC-GSH** after incubation with GGT. Given these results, a possible sensing mechanism for the activation of **CFC-GSH** with GGT was proposed (Fig. 2a). Upon GGT-induced cleavage of the γ-glutamyl bond on probe **CFC-GSH**, the released amino group in the cysteinyl-glycine residue promotes an intramolecular cascade arrangement of thiolate, yielding amino-substituted **CFC-NCS** through a five-membered cyclic transition state. Consequently, the absorption and fluorescence spectra of **CFC-GSH** exhibited a distinct bathochromic shift upon incubation with GGT.

In vitro characterization

After that, the sensing kinetics of **CFC-GSH** toward GGT was further investigated. As shown in Fig. 1h, the fluorescence ratio signals (F_{660}/F_{930}) of **CFC-GSH** increased over incubation time and arrived at a plateau in 22 min, indicative of the fast response to GGT. To visualize the fluorescence changes, the response progression of **CFC-GSH** to GGT was imaged using a full spectrum animal *In Vivo* Imaging System (IVIS). As shown in Fig. 1g, the NIR-II fluorescence signal of GGT-treated **CFC-GSH** solution gradually weakened with the extension of incubation time, while the NIR-I fluorescence signal gradually enhanced. The results indicate that **CFC-GSH** could be an ideal tool for rapid detection and imaging of GGT.

The specificity of **CFC-GSH** was assessed in the presence of potential biological interferents including 10% fetal bovine
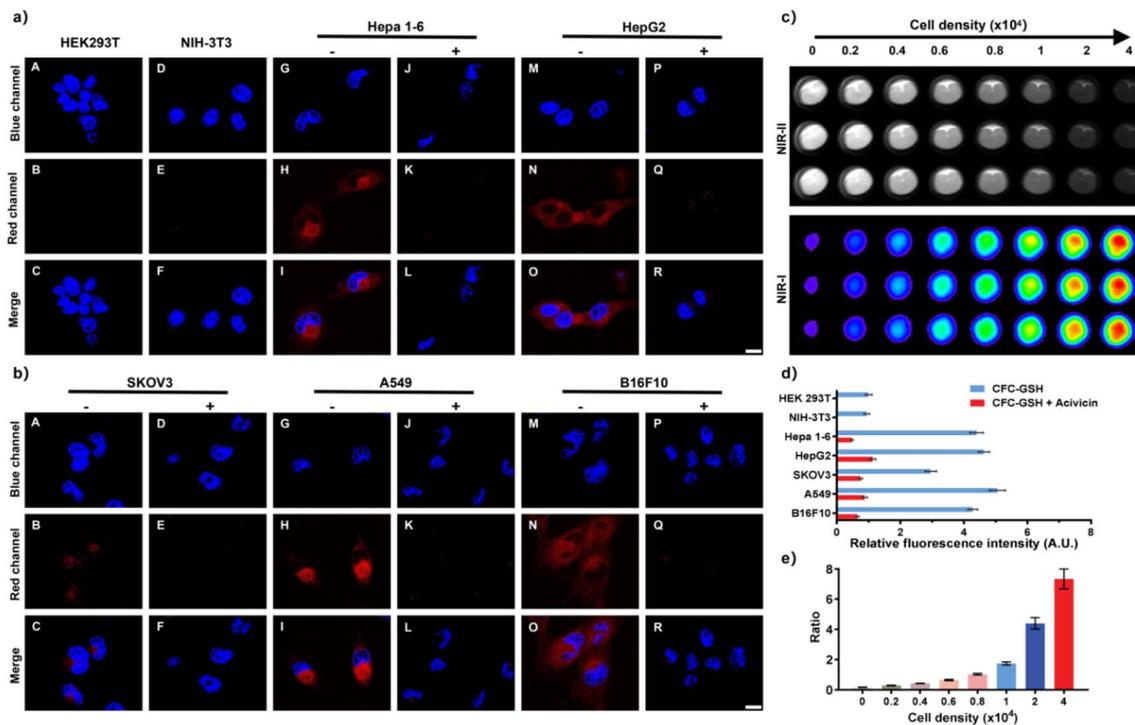
Fig. 3 Fluorescence imaging of (a) normal cells, HCC and (b) other cancer cells incubated with **CFC-GSH** (5 μM, 0.5% DMSO) for 30 min and then treated with Hoechst (1 μM) for another 5 min. (J–L) Hepa 1–6, (P–R) HepG2 cells in (a) (D–F) SKOV3, (J–L) A549, and (P–R) HepG2 cells in (b) pretreated with acivicin (1 mM) for 30 min. Blue channel: $\lambda_{ex} = 405$ nm and $\lambda_{em} = 430–480$ nm; red channel: $\lambda_{ex} = 620$ nm and $\lambda_{em} = 650–700$ nm. Scale bar: 10 μm. (c) NIR-II (upper panel, $\lambda_{ex} = 808$ nm) and NIR-I (lower panel, $\lambda_{ex} = 605$ nm) fluorescence images of **CFC-GSH** (5 μM, 0.5% DMSO) upon incubation with Hepa 1–6 cells at 37 °C for 30 min. (d) Relative fluorescence intensity of **CFC-GSH**-incubated cells in (a) and (b) and the intensity of image B in (a) are set as 1.0. (e) The corresponding quantitative analysis of ratiometric fluorescence intensity in (c). Data are presented as mean ± s.d. ($n = 3$).

serum (FBS), enzymes (NTR, APN, ALP, Try, CE, and GOx) and amino acids (Glu and Cys). As shown in Fig. S9a,† no significant fluorescence alteration in both NIR-II and NIR-I channels can be triggered by the biological interferents. Moreover, the presence of these interferents also showed no obvious interference with the GGT-triggered fluorescence changes (Fig. S9b†), demonstrating the potential of **CFC-GSH** to specifically identify GGT in complex biological samples. Furthermore, the presence of amino acids (Hcy, Iso, Leu, Arg, Lys and Phe), cations (Na$^+$, K$^+$, Mg^{2+}, Ca^{2+}, Al^{3+}, and Fe^{2+}) and anions (H$_2$PO$_4^-$, NO$_3^-$, and CO$_3^{2-}$) also exhibited limited interference in the detection of GGT (Fig. S10†), indicating the excellent selectivity of **CFC-GSH**. In addition, the photostability of **CFC-GSH** was examined with the excitation of a 150 W xenon lamp. As shown in Fig. S11,† the fluorescence intensity ratio (F_{660}/F_{930}) of **CFC-GSH** remained relatively stable during the scanning period of 8000 s, indicative of the desirable resistance to photobleaching. These results suggested that **CFC-GSH** holds great potential for accurate detection of GGT activity in practical settings.

Fluorescence imaging in living cells

Inspired by the favourable performance *in vitro*, we subsequently assessed the applicability of **CFC-GSH** in living cells. Before that, **CFC-GSH** was invoked to evaluate its biocompatibility with cell lines (HEK293T and HepG2 cells). As shown in

Fig. S12,† after incubation with various concentrations of **CFC-GSH** (0–50 μM) for 24 h, the cell viability of all cells remained at a high level (over 85%), suggesting the good biocompatibility of **CFC-GSH**. Given the GGT-triggerable NIR-I fluorescence enhancement, the fluorescence imaging of **CFC-GSH** in different cell lines was carried out using a confocal laser scanning microscope (CLSM). As depicted in Fig. 3a, faint fluorescence signals were observed in human embryonic kidney cells (HEK293T) and mouse embryonic fibroblast cells (NIH-3T3), which suggests that GGT activity remains negligible in normal cells. By contrast, intensive NIR-I fluorescence signals were observed in hepatocellular carcinoma cells (human HepG2 and murine Hepa 1–6), which were 4.63 and 4.40 times higher than those in normal cells, respectively, suggesting higher GGT levels in HCC (Fig. 3d). When the cancer cells were pretreated with GGT inhibitor acivicin (1 mM), the NIR-I fluorescence signals decreased drastically, elucidating the fact that the fluorescence change comes from the GGT-catalysed cleavage of the γ-glutamyl bond in **CFC-GSH** (Fig. 3a and b). Furthermore, other cancer cells of different origins were also demonstrated with different GGT levels according to the activated NIR-I fluorescence intensity (Fig. 3b). These results verified the capability of **CFC-GSH** for evaluating the GGT levels in living cells, thus providing the accessibility for differentiating cancer cells from normal cells.
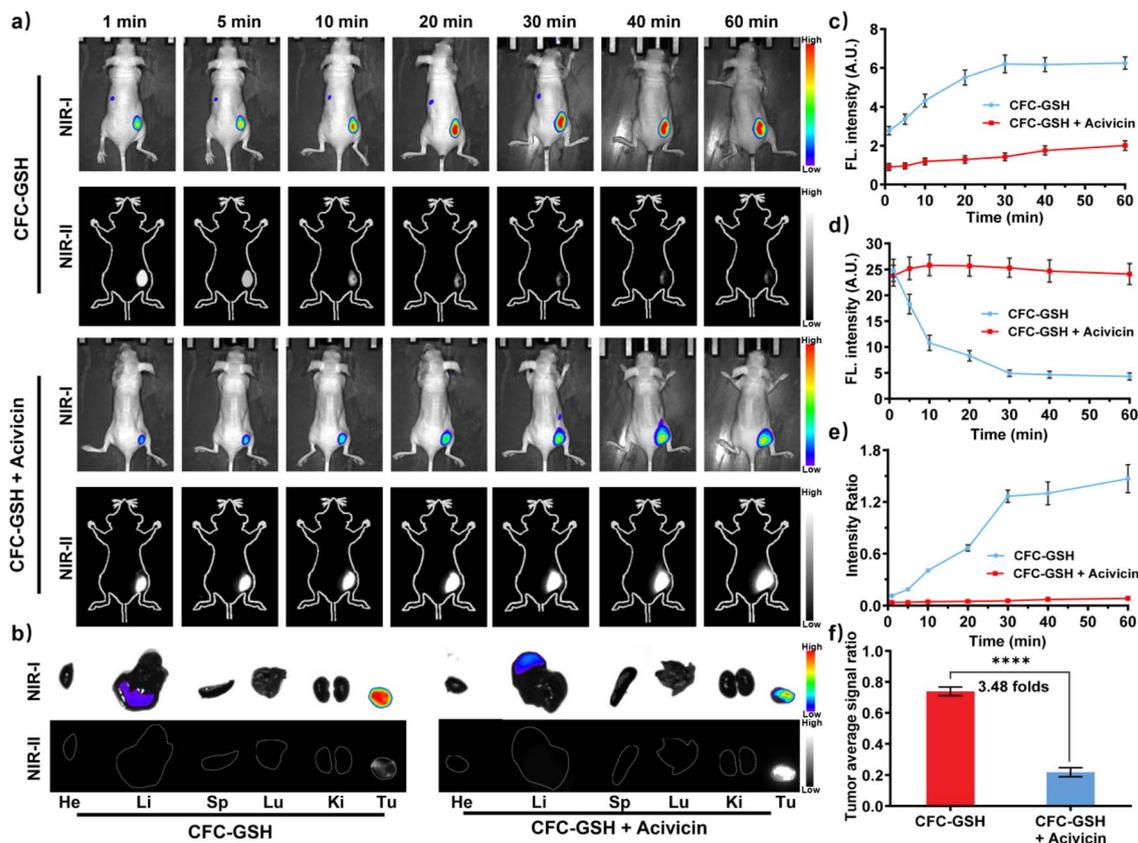
Fig. 4 (a) NIR-I ($\lambda_{ex} = 605$ nm, $\lambda_{em} = 660$ nm) and NIR-II ($\lambda_{ex} = 808$ nm, 1075 nm LP) fluorescence imaging of tumour–bearing BALB/c nude mice at different times (1, 5, 10, 20, 30, 40, and 60 min) after intratumoural injection of **CFC-GSH** (50 μL, 10 μM in PBS) without/with pretreatment of acivicin (1 mM) for another 30 min. (b) NIR-I and NIR-II fluorescence imaging of the isolated organs from the mice in (a). (c–e) Time-dependent quantitative statistics of (c) NIR-I and (d) NIR-II fluorescence intensity, and (e) the corresponding fluorescence intensity ratio of the mice in (a). (f) Quantitative biodistribution analysis of the mean fluorescence intensity ratio in tumours and major organs. Data are presented as mean ± s.d. (*n* = 3). ****$p < 0.0001$.

Considering the desirable ratiometric response of probe **CFC-GSH**, the possibility of quantitative detection of endogenous GGT produced by the density gradients of cancer cells was further explored. The Hepa 1–6 cells were pre-transferred into a black 96-well plate with controlled densities, followed by incubation with **CFC-GSH** for 30 min and the signals were recorded using the IVIS. As shown in Fig. 3c and e, the fluorescence signals in the NIR-II channel exhibited a density-dependent decline process, whereas the signals in the NIR-I channel exhibited a gradual enhancement process. Moreover, a good linear relationship was found between the fluorescence intensity ratio and cell number from 2000 to 40 000 per well ($R^2 = 0.9723$) with a LOD lower than 320 cells ($3\sigma/k$), showing the feasibility of **CFC-GSH** for quantitatively evaluating GGT activities in cancer cells (Fig. S13†). These results suggest that probe **CFC-GSH** provided a promising tool for discriminating GGT-overexpressed cancer cells from other cells.

Dual-channel imaging of subcutaneous tumours

Next, the ratiometric probe **CFC-GSH** was further employed for real-time *in vivo* visualization of GGT activity in tumour-bearing mice to monitor HCC. A murine hepatocellular carcinoma xenograft tumour model was established by subcutaneously injecting Hepa 1–6 cells into the assigned site of female BALB/C nude mice.[57] After 2 weeks, the tumour grew about 100 mm³ and was then treated with **CFC-GSH** for NIR-I and NIR-II dual-channel imaging using the IVIS. As exhibited in Fig. 4a and c, distinct NIR-I fluorescence was collected specifically in the tumour region within 1 min and gradually increased to the maximum within 30 min, while, in the NIR-II channel, the signal intensities dropped significantly in the imaging period, indicating the rapid activation of **CFC-GSH** *in situ* (Fig. 4a and d). The fluorescence intensity ratio increased in a time-dependent manner and reached a plateau at 30 min (Fig. 4e). To validate the finding that fluorescence changes were indeed triggered by GGT in subcutaneous tumours, the mice were preinjected with inhibitor acivicin for 30 min and then treated orthotopically with **CFC-GSH**. As shown in Fig. 4a, the enhancement of NIR-I fluorescence and the decline of NIR-II fluorescence in the tumour region were blocked well by acivicin. The fluorescence intensity ratio in the HCC tumour attenuated 19.52-fold compared with that in the absence of acivicin, verifying that the dual-channel fluorescence changes at the
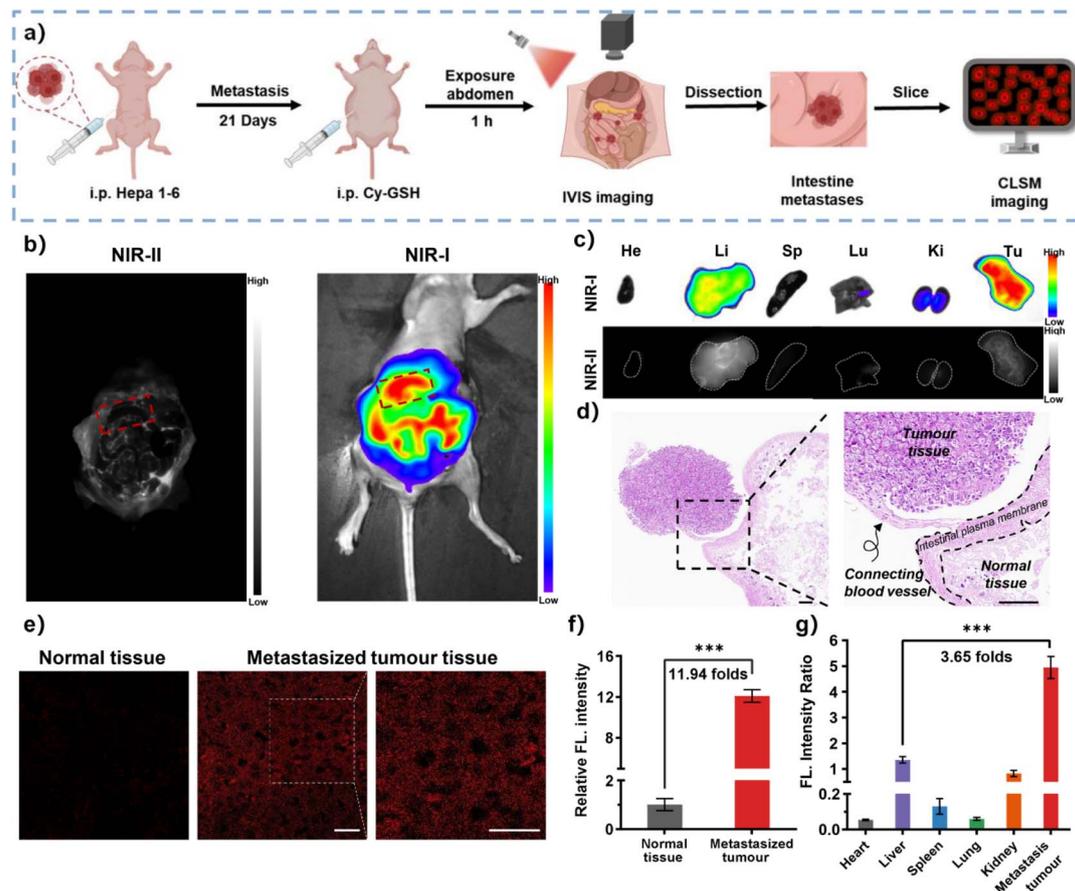
Fig. 5 (a) Schematic diagram of constructing and identifying abdominal tumour metastases in BALB/c nude mice. (b) *In vivo* NIR-I (λ_{ex} = 605 nm, λ_{em} = 660 nm) and NIR-II (λ_{ex} = 808 nm, 1075 nm LP) fluorescence imaging of the dissected mice bearing Hepa 1–6 abdominal tumour metastases after intraperitoneal injection **CFC-GSH** (100 μL, 20 μM in PBS) for 1 h. (c) *Ex vivo* NIR-I and NIR-II fluorescence imaging of the organs and peritoneal metastasized tumours isolated from the mice. (d) H&E staining of the tumour margins on the mesentery. Scale bars: 100 μm. Fluorescence confocal images (e) and the corresponding relative fluorescence intensity (f) of **CFC-GSH** (100 μL, 10 μM in PBS) in normal intestinal and metastases tissue slices. Scale bar: 20 μm. (g) The corresponding quantitative statistics of the mean fluorescence intensity ratio of the isolated organs in (c). Data are presented as mean $\pm$ s.d. (n = 3). ***p < 0.001.

tumour site resulted from selective cleavage of **CFC-GSH** by GGT (Fig. 4a and e). Furthermore, *ex vivo* fluorescence images of the tumour and main organs (heart, liver, spleen, lung, and kidney) were recorded after sacrificing the mice at 2 h post-injection. As shown in Fig. 4b, faint NIR-II fluorescence signals but intensive NIR-I fluorescence signals were observed only in tumours, suggesting the specific fluorescence changes triggered by tumoral GGT. Consistent with the *in vivo* results, the fluorescence changes were attenuated as well by the inhibitor, with a decrease in the fluorescence intensity ratio of about 3.48-fold (Fig. 4f). Moreover, the tissue sections were obtained to explore the accessibility of **CFC-GSH** in tissue imaging. As shown in Fig. S14,† in contrast to the negligible fluorescence in liver slices, stronger fluorescence was observed in tumours with a 12.86-fold signal enhancement, suggesting that **CFC-GSH** has the potential to discriminate tissues with high GGT expression from those with low expression. These results were in keeping with those *in vitro*, supporting the superiority of **CFC-GSH** to reflect the dynamic level changes of GGT in HCC xenograft mice.

Dual-channel imaging of metastasis tumours

Most malignant cancers, including HCC, tend to metastasize from the primary site to secondary sites within the host.[5,58,59] Patients with advanced HCC should be carefully monitored due to the frequent occurrence of extrahepatic metastases, including those in the lungs, lymph nodes, and peritoneal metastases.[60] However, metastasized tumours are often difficult to detect and are located early due to their small size and deep location within the body.[33,61] To mimic metastasis of HCC to the abdominal cavity, Hepa 1–6 cells were injected into the abdominal cavity of female BALB/C nude mice, and 3 weeks later the probe was administrated *via* intraperitoneal injection. After 1 h, the abdominal cavity of mice was exposed to dual-channel imaging (Fig. 5a). As shown in Fig. 5b, the peritoneal metastasized tumours in the abdominal cavity could be observed at the intestinal plasma membrane according to the fluorescence signals from two channels, suggesting that HCC tumours predominantly metastasized to the intestines. Hae-matoxylin–eosin (H&E) stained tissue specimens revealed
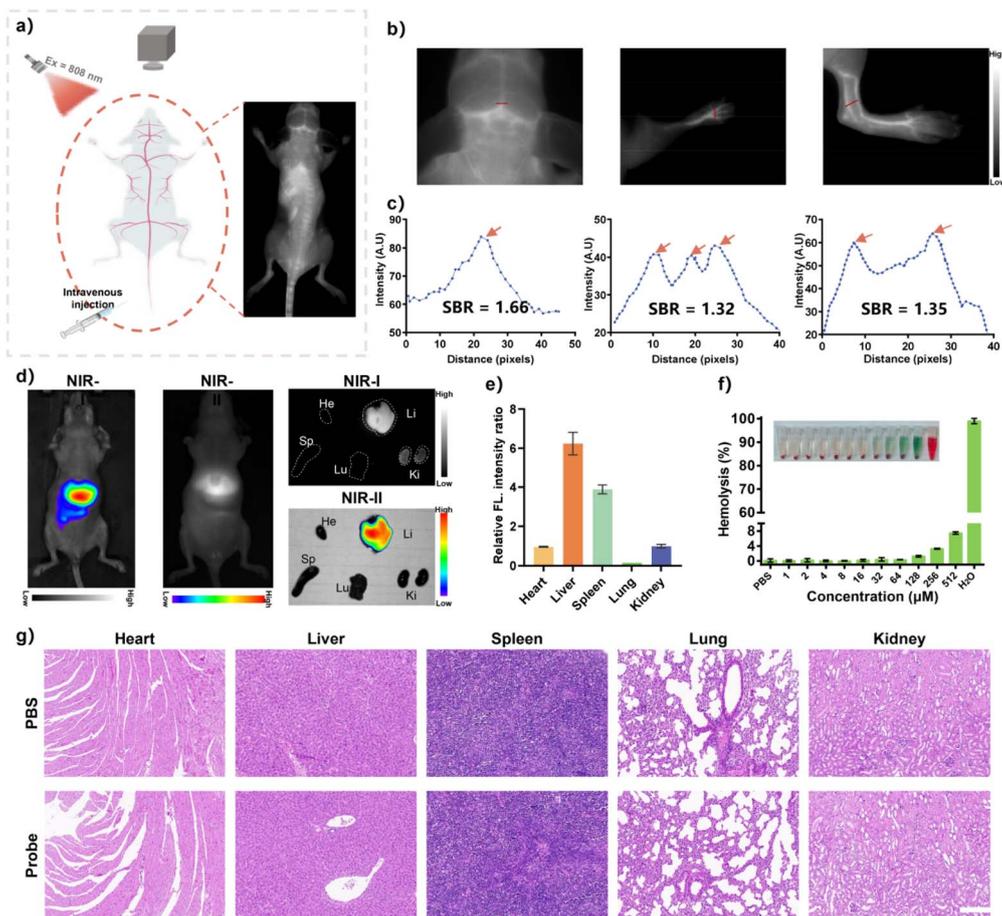
Fig. 6 (a) Schematic of vascular imaging and the NIR-II fluorescence image within living mice after i.v. injection of **CFC-GSH** (200 μL, 80 μM in PBS), acquired in the prostrate ($\lambda_{ex} = 808$ nm, 1075 nm LP). (b) NIR-II vascular imaging of the brain, paw and hindlimb after i.v. injection of **CFC-GSH**. (c) The corresponding cross-sectional fluorescence intensity profiles were measured along positions marked by the red lines in the three ROI regions in (b). (d) NIR-I ($\lambda_{ex} = 605$ nm) and NIR-II ($\lambda_{ex} = 808$ nm) fluorescence images of the mice and the isolated organs (heart, liver, spleen, lung, and kidney) after intravenous injection with **CFC-GSH** (200 μL, 80 μM in PBS) for 24 h. (e) The corresponding relative quantitative statistics of the mean fluorescence intensity ratio of the isolated organs in (d) and the ratio of the kidney are set at 1.0. (f) Homolysis rate of **CFC-GSH** at different concentrations from 1 to 512 μM incubated with red blood cells for 2 h at 37 °C, using pure water as a positive control and PBS buffer as a negative control. (g) H&E staining of vital organs (heart, liver, spleen, lung, and kidney) harvested from mice after intravenous injection with PBS or **CFC-GSH** for 24 h, respectively. Scale bar: 200 μm. Data are presented as mean ± s.d. ($n = 3$).

tumorous regions adjacent to normal intestine regions, connected by a blood vessel, which was distinguishable by the cellular morphology (Fig. 5d). Following the sacrifice of the mice, the intestinal tissue of interest and the main organs were collected for *ex vivo* fluorescence imaging. The results showed that intensive NIR-I fluorescence and faint NIR-II fluorescence were only found in tumour-containing intestinal tissue (Fig. 5c). Notably, while the liver exhibited significant NIR-I fluorescence, the NIR-II fluorescence was much higher in the liver than in tumour tissues. This discrepancy can be attributed to the excessive uptake of probes by the liver and subsequent enzymatic catalysis of endogenous GGT. The fluorescence ratio allowed for self-calibration of signals in the liver, enabling specific detection and tracking of peritoneal metastasis of HCC *in vivo*. This result highlights the advantages of the ratiometric response mode provided by the probe **CFC-GSH** (Fig. 5g). Furthermore, fluorescence imaging of metastatic tumour sections showed that tumour tissues displayed high-contrast

fluorescence, with fluorescence intensity 12.1 times that of normal intestinal tissues (Fig. 5e). This indicates the excellent imaging capability of **CFC-GSH** for *in vivo* detection of HCC intestinal metastases (Fig. 5f). Collectively, **CFC-GSH** shows potential as a tool for accurate imaging of metastatic tumours in clinical applications.

Fluorescence angiography with CFC-GSH

From the perspective of broader application scenarios, we would like to highlight the innate NIR-II signals of **CFC-GSH** in fluorescence imaging of systemic circulation vessels. The fluorescence in the NIR-II window offers several advantages, including optimized spatial resolution, improved imaging depth, a high signal-to-background ratio (SBR), and reduced tissue autofluorescence, thereby providing non-invasive, high-resolution imaging at millimetre depths within biological tissues.[36,62,63] As demonstrated in Fig. 6a and b, bright NIR-II fluorescence delineated the blood vessels within minutes

following intravenous injection of **CFC-GSH**, clearly visualizing the blood circulatory system in nude mice with high spatial resolution. Impressively, the SBR of vascular signals in the brain, paw, and hindlimb of living mice were quantified as 1.66, 1.32, and 1.35 (Fig. 6c), respectively, indicating that **CFC-GSH** holds potential for non-invasive imaging of subcutaneous vasculature in live mice. These results demonstrate the superiority of **CFC-GSH** bioimaging in the NIR-II window, making it a valuable tool for *in vivo* microangiography and disease monitoring.

To investigate its biodistribution, *in vivo* fluorescence images were recorded from both NIR-I and NIR-II channels using the IVIS at 24 h after intravenous injection of **CFC-GSH**. As shown in Fig. 6d, strong fluorescence signals were observed in the liver in both channels, indicating that liver metabolism serves as a primary clearance pathway for **CFC-GSH**. Subsequently, the mice were sacrificed, and their main organs were collected for dual-channel imaging. As shown in Fig. 6e, the intensive NIR-II fluorescence was recorded in the liver, with weaker NIR-II signals also detected in the spleen. In contrast, NIR-I signals were only found in the liver, which has innate expression of GGT, further verifying the optimized specificity of **CFC-GSH**-supported ratiometric mode. To evaluate the biocompatibility of **CFC-GSH**, H&E staining of the organ slices was performed. The results showed no obvious pathological damage or lesions (Fig. 6g), suggesting low systematic toxicity of the probe to normal organs and tissues. Consistent with the result, no significant haemolysis occurred at a concentration reaching 512 μM (Fig. 6f). Collectively, these results validated the reliable biocompatibility of **CFC-GSH** for imaging species of interest in living things.

Conclusions

This work presents a ground-breaking approach for modulating the NIR-II fluorescence of anionic cyanine-based scaffolds using a specific enzymatic trigger. This strategy not only provides a powerful tool for HCC localization but also signifies a valuable approach for developing enzyme-activated NIR-II probes for broader cancer diagnosis and management. Based on the pioneering strategy, **CFC-GSH**-boosted dual-channel imaging enables real-time monitoring of GGT activity in tumours and precise localization of metastatic HCC lesions within the abdomen. Importantly, the self-calibration properties of the ratiometric probe **CFC-GSH** diminish interference from innate GGT activities in the liver. Given its inherent NIR-II fluorescence, we also demonstrated the potential application of **CFC-GSH** in fluorescence microangiography in the NIR-II window. Notably, **CFC-GSH** exhibits no acute toxicity, suggesting its potential for future clinical application in HCC tumour staging, localization, and treatment decision-making.

Experimental section

Synthesis and measurement methods

CFC-GSH was synthesized *via* three steps, and the specific information of relative compounds is given in the ESI.† The

further details of *in vitro* detection and the cell treatment and imaging are available in the ESI.†

Methods of theoretical calculations

Calculations of optimal geometries and electronic structures of **CFC-GSH** and **CFC-NCS** were carried out using density functional theory (DFT) at the b3lyp/6-31g(d) level.[52] The starting structures with different conformational isomers were considered to ensure that the optimized structure corresponds to a global minimum. All these calculations were carried out with Gaussian 16 software (water was employed in all the calculations). The obtained data were analysed using GaussView 5.0 software.

Method of molecular docking simulation

Molecular docking simulations were carried out on MOE2019 software. The crystal structure of human glutaminase in complex with L-glutamine (PDB ID: 3VP0)[55] was downloaded from RCSB PDB and underwent a series of optimizations (completing the protein sequence, deleting repeated subunits, adding hydrogen atoms, and removing all water molecules and ligands). Different conformations of **CFC-GSH** were searched ($n = 10\,000$) and the docking cycles and the parameters between the ligand and protein were set according to the defaults.

Animal models and fluorescence imaging

BALB/c nude mice (female, 6 weeks old) were obtained from the Animal Centre of Xiangya Medical School, Central South University. All animal procedures complied with the Guide for the Care and Use of Laboratory Animals and were approved (application number: XMXH-2023-1384) by the Laboratory Animal Welfare Ethics Committee, Central South University, China.

Cells were pelleted by centrifugation and resuspended in pre-cooled sterile PBS. For subcutaneous tumours, 150 μL PBS containing Hepa 1–6 cells (1×10^6) were implanted subcutaneously into the Balb/c nude mice. After two weeks, the tumour grew about 100 mm³ and the mice were submitted to tumour imaging after being randomly allocated into two groups. In the experimental group, probe **CFC-GSH** (50 μL, 10 μM in PBS, containing 1% DMSO) was intratumorally injected into the tumour site. In the inhibitor group, the tumour was pretreated with acivicin (1 mM) for 30 min and then treated with **CFC-GSH**. The *in vivo* fluorescence images were obtained at different times (1, 5, 10, 20, 30, 40, and 60 min) by using the full spectrum animal *In Vivo* Imaging System (IVIS) after injection. Then, the mice were sacrificed and dissected after 2 h post-injection to collect major organs including the heart, liver, spleen, lung, and kidney and the tumour for fluorescence imaging.

For metastasis tumours in the abdomen, 200 μL PBS containing Hepa 1–6 cells (5×10^6) were implanted intraperitoneally into the Balb/c nude mice. After three weeks, the hepatocarcinoma ascites formed, and the probe **CFC-GSH** (100 μL, 20 μM in PBS, containing 1% DMSO) was intraperitoneally in the mice. After one hour, mice were sacrificed and dissected to expose the abdominal cavity for fluorescence imaging using

the IVIS, and major organs including the heart, liver, spleen, lung, and kidney and part of the intestine were removed for fluorescence imaging.

IVIS spectral imaging system

For NIR-I fluorescence imaging of the samples, the fluorescence images were acquired upon excitation at 605 nm, and the collected emission was 660 nm. For NIR-II fluorescence imaging of the samples, the fluorescence images were acquired upon excitation at 808 nm, and a 1075 nm long-pass filter was used for collecting the fluorescent signals. The light intensities for NIR-I and NIR-II fluorescence imaging were set to 70% and 80%, respectively.

In vivo vascular imaging

Before the experiment, mice were anesthetized under a continuous 2% isoflurane atmosphere. For whole-body vascular imaging, the mice were intravenously injected with **CFC-GSH** (200 μL, 80 μM in PBS, containing 1% DMSO) and then were imaged immediately by using the full spectrum animal *In Vivo* Imaging System (IVIS). The excitation laser was at 808 nm and the emission was collected using 1075 nm filters. The light intensity was set to 80%, with an exposure time of 20 ms.

Data availability

Additional experimental details and data are provided in the ESI.†

Author contributions

Feiyi Chu: conceptualization, investigation, methodology, writing – original draft. Bin Feng: investigation, validation, writing – review & editing. Yiyang Zhou: formal analysis, investigation, validation. Min Liu: resources, formal analysis, writing – review & editing, validation. Hailiang Zhang: formal analysis, resources. Meihui Liu: validation, writing – review & editing, resources. Qian Chen: resources, validation. Shengwang Zhang: formal analysis, methodology. Yeshuo Ma: resources, validation. Jie Dong: formal analysis, software. Fei Chen: validation, resources, writing – review & editing. Wenbin Zeng: supervision, conceptualization, funding acquisition, writing – review & editing.

Conflicts of interest

There are no conflicts to declare.

Acknowledgements

Notes and references

1 Y. Zhang, Z. Zhang, M. Wu and R. Zhang, *ACS Meas. Sci. Au*, 2024, **4**, 54–75.

2 B. Feng, F. Chu, Y. Fang, M. Liu, X. Feng, J. Dong, F. Chen and W. Zeng, *Chem. Sci.*, 2024, **15**, 7324–7331.

3 C. Chen, X. Zhang, Z. Gao, G. Feng and D. Ding, *Nat. Protoc.*, 2024, **19**, 2408–2434.

4 J. Qi, X. Duan, Y. Cai, S. Jia, C. Chen, Z. Zhao, Y. Li, H.-Q. Peng, R. T. K. Kwok, J. W. Y. Lam, D. Ding and B. Z. Tang, *Chem. Sci.*, 2020, **11**, 8438–8447.

5 H. Lou, A. Ji, C. Qu, S. Duan, H. Liu, H. Chen and Z. Cheng, *Chem. Eng. J.*, 2022, **449**, 137848–137856.

6 Y. Yue, T. Zhao, Z. Xu, W. Chi, X. Chai, J. Ai, J. Zhang, F. Huo, R. M. Strongin and C. Yin, *Adv. Sci.*, 2022, **10**, 2205080–2205090.

7 A. Ji, H. Lou, J. Li, Y. Hao, X. Wei, Y. Wu, W. Zhao, H. Chen and Z. Cheng, *Chem. Sci.*, 2024, **15**, 3339–3348.

8 Y. Lai, Y. Dang, Q. Sun, J. Pan, H. Yu, W. Zhang and Z. Xu, *Chem. Sci.*, 2022, **13**, 12511–12518.

9 Y. Zhang, G. Zhang, Z. Zeng and K. Pu, *Chem. Soc. Rev.*, 2022, **51**, 566–593.

10 X. Zhang, S. Li, H. Ma, H. Wang, R. Zhang and X.-D. Zhang, *Theranostics*, 2022, **12**, 3345–3371.

11 J. Bao, R. Liu, Z. Yu, Z. Cheng and B. Chang, *Adv. Funct. Mater.*, 2024, **34**, 2316646–2316661.

12 J. Ouyang, L. Sun, Z. Zeng, C. Zeng, F. Zeng and S. Wu, *Angew. Chem., Int. Ed.*, 2020, **59**, 10111–10121.

13 Z. Qin, T. B. Ren, H. Zhou, X. Zhang, L. He, Z. Li, X. B. Zhang and L. Yuan, *Angew. Chem., Int. Ed.*, 2022, **61**, e202201541–e202201549.

14 L. Shen, J. Li, C. Wen, H. Wang, N. Liu, X. Su, J. Chen and X. Li, *Sci. Adv.*, 2024, **10**, eado2037–eado2051.

15 J.-A. Chen, H. Pan, Z. Wang, J. Gao, J. Tan, Z. Ouyang, W. Guo and X. Gu, *Chem. Commun.*, 2020, **56**, 2731–2734.

16 I. Castellano and A. Merlino, *Cell. Mol. Life Sci.*, 2012, **69**, 3381–3394.

17 Z.-Y. Hu, X.-Y. Chen, Y.-S. Yang, S.-J. Wang, Z.-G. Hu and K. Wang, *Coord. Chem. Rev.*, 2024, **501**, 215562–215587.

18 Y. Liu, B. Feng, X. Cao, G. Tang, H. Liu, F. Chen, M. Liu, Q. Chen, K. Yuan, Y. Gu, X. Feng and W. Zeng, *Analyst*, 2019, **144**, 5136–5142.

19 D. Yao, D. Jiang, Z. Huang, J. Lu, Q. Tao, Z. Yu and X. Meng, *Cancer*, 2000, **88**, 761–769.

20 X. Wang, S. He, P. Cheng and K. Pu, *Adv. Mater.*, 2023, **35**, 2206510–2206518.

21 S.-J. Wu, Y.-X. Lin, H. Ye, X.-Z. Xiong, F.-Y. Li and N.-S. Cheng, *Int. J. Surg.*, 2016, **36**, 143–151.

22 K. Wang, X.-Y. Chen, W.-D. Liu, Y. Yue, X.-L. Wen, Y.-S. Yang, A.-G. Zhang and H.-L. Zhu, *Anal. Chem.*, 2023, **95**, 14235–14243.

23 M. Orlowski and A. Meister, *Biochim. Biophys. Acta, Spec. Sect. Enzymol. Subj.*, 1963, **73**, 679–681.

24 S. Ye, S. Wang, D. Gao, K. Li, Q. Liu, B. Feng, L. Qiu and J. Lin, *Bioconjugate Chem.*, 2020, **31**, 174–181.

25 K. Kiuchi, K. Kiuchi, T. Nagatsu, A. Togari and H. Kumagai, *J. Chromatogr. A*, 1986, **357**, 191–198.

26 Z. Hai, Y. Ni, D. Saimi, H. Yang, H. Tong, K. Zhong and G. Liang, *Nano Lett.*, 2019, **19**, 2428–2433.

27 Q. Liu, J. Yuan, R. Jiang, L. He, X. Yang, L. Yuan and D. Cheng, *Anal. Chem.*, 2023, **95**, 2062–2070.

28 K. Wang, X.-Y. Chen, B. Zhang, Y. Yue, X.-L. Wen, Y. Yang, Y.-S. Yang, H.-L. Zhu, H.-J. Liu and A.-G. Zhang, *Biosens. Bioelectron.*, 2023, **241**, 115721–115728.

29 K. Li, Y. Lyu, Y. Huang, S. Xu, H.-W. Liu, L. Chen, T.-B. Ren, M. Xiong, S. Huan, L. Yuan, X.-B. Zhang and W. Tan, *Proc. Natl. Acad. Sci. U. S. A.*, 2021, **118**, e2018033118–e2018033127.

30 Y. Liu, J. Tan, Y. Zhang, J. Zhuang, M. Ge, B. Shi, J. Li, G. Xu, S. Xu, C. Fan and C. Zhao, *Biomaterials*, 2018, **173**, 1–10.

31 K. Wang, W. Wang, X.-Y. Chen, Y.-S. Yang and H.-L. Zhu, *Biosens. Bioelectron.*, 2023, **219**, 114767–114714.

32 H. Li, Q. Yao, F. Xu, N. Xu, R. Duan, S. Long, J. Fan, J. Du, J. Wang and X. Peng, *Biomaterials*, 2018, **179**, 1–14.

33 J. Ou-Yang, Y. Li, W.-L. Jiang, S.-Y. He, H.-W. Liu and C.-Y. Li, *Anal. Chem.*, 2019, **91**, 1056–1063.

34 H. Chen, Z. Cai, J. Gui, Y. Tang, P. Yin, X. Zhu, Y. Zhang, H. Li, M. Liu and S. Yao, *J. Mater. Chem. B*, 2023, **11**, 1279–1287.

35 Y.-L. Qi, Y.-Z. Li, M.-J. Tan, F.-F. Yuan, N. Murthy, Y.-T. Duan, H.-L. Zhu and S.-Y. Yang, *Coord. Chem. Rev.*, 2023, **486**, 215130–215167.

36 R. Xu, D. Jiao, Q. Long, X. Li, K. Shan, X. Kong, H. Ou, D. Ding and Q. Tang, *Biomaterials*, 2022, **289**, 121780–121792.

37 M. Jiang, Q. Ma, J. Huang, S. Bi and S. Zeng, *Chem. Eng. J.*, 2023, **475**, 145977–145984.

38 F. Wang, Y. Zhu, L. Zhou, L. Pan, Z. Cui, Q. Fei, S. Luo, D. Pan, Q. Huang, R. Wang, C. Zhao, H. Tian and C. Fan, *Angew. Chem., Int. Ed.*, 2015, **54**, 7349–7353.

39 R. Obara, M. Kamiya, Y. Tanaka, A. Abe, R. Kojima, T. Kawaguchi, M. Sugawara, A. Takahashi, T. Noda and Y. Urano, *Angew. Chem., Int. Ed.*, 2020, **60**, 2125–2129.

40 S. M. Usama, F. Inagaki, H. Kobayashi and M. J. Schnermann, *J. Am. Chem. Soc.*, 2021, **143**, 5674–5679.

41 H. Tong, Y. Zheng, L. Zhou, X. Li, R. Qian, R. Wang, J. Zhao, K. Lou and W. Wang, *Anal. Chem.*, 2016, **88**, 10816–10820.

42 R. Huo, X. Zheng, W. Liu, L. Zhang, J. Wu, F. Li, W. Zhang, C.-S. Lee and P. Wang, *Chem. Commun.*, 2020, **56**, 10902–10905.

43 B. Feng, F. Chu, A. Bi, X. Huang, Y. Fang, M. Liu, F. Chen, Y. Li and W. Zeng, *Biotechnol. Adv.*, 2023, **68**, 108244.

44 Y. Ma, L. Liu, Z. Ye, L. Xu, Y. Li, S. Liu, G. Song and X.-B. Zhang, *Sci. Bull.*, 2023, **68**, 2382–2390.

45 P.-A. Bouit, D. Rauh, S. Neugebauer, J. L. Delgado, E. D. Piazza, S. Rigaut, O. Maury, C. Andraud, V. Dyakonov and N. Martin, *Org. Lett.*, 2009, **11**, 4806–4809.

46 Z. a. Li, S. Mukhopadhyay, S.-H. Jang, J.-L. Brédas and A. K. Y. Jen, *J. Am. Chem. Soc.*, 2015, **137**, 11920–11923.

47 Y. Li, Y. Zhou, X. Yue and Z. Dai, *Bioact. Mater.*, 2021, **6**, 794–809.

48 L.-Y. Niu, Y.-S. Guan, Y.-Z. Chen, L.-Z. Wu, C.-H. Tung and Q.-Z. Yang, *J. Am. Chem. Soc.*, 2012, **134**, 18928–18931.

49 R. Song, Y. Dong, Z. Zhong, Q. Zhao, Y. Hu, M. Lei, P. Lei, Z. Jiang, K. Qian, C. Shi, Z. He, Y. Qin, J. Wang and H. Chen, *J. Med. Chem.*, 2024, **67**, 10275–10292.

50 P. Wu, Z. Qu, J. Zhang, X. Ren, D. Wang, C. Huang, K. Cheng, J. Qi, H. Shi, S. Gan, W. Wei, Y. Zhang, C.-S. Lee, L. Wang and H. Sun, *Adv. Funct. Mater.*, 2024, 2400597–2400607.

51 J. B. King, M. B. West, P. F. Cook and M. H. Hanigan, *J. Biol. Chem.*, 2009, **284**, 9059–9065.

52 K. Thangavelu, Q. Y. Chong, B. C. Low and J. Sivaraman, *Sci. Rep.*, 2014, **4**, 3827–3833.

53 X. Zhou, Y. Liu, Q. Liu, L. Yan, M. Xue, W. Yuan, M. Shi, W. Feng, C. Xu and F. Li, *Theranostics*, 2019, **9**, 4597–4607.

54 B. Feng, Y. Liu, S. Huang, X. Huang, L. Huang, M. Liu, J. Wu, T. Du, S. Wang, X. Feng and W. Zeng, *Sens. Actuators, B*, 2020, **325**, 128786–128795.

55 Y. Li, T. Ma, H. Jiang, W. Li, D. Tian, J. Zhu and Z. a. Li, *Angew. Chem., Int. Ed.*, 2022, **61**, e202203093–e202203099.

56 F. Chu, B. Feng, M. Liu, M. Liu, F. Chen, J. Dong and W. Zeng, *Dyes Pigm.*, 2024, **222**, 111894–111900.

57 Y. Wen, N. Jing, M. Zhang, F. Huo, Z. Li and C. Yin, *Adv. Sci.*, 2023, **10**, 2206681–2206690.

58 Y.-Y. Zhu, L. Song, Y.-Q. Zhang, W.-L. Liu, W.-L. Chen, W.-L. Gao, L.-X. Zhang, J.-Z. Wang, Z.-H. Ming, Y. Zhang and G.-J. Zhang, *Cancer Res.*, 2023, **83**, 3428–3441.

59 J. M. Llovet, R. K. Kelley, A. Villanueva, A. G. Singal, E. Pikarsky, S. Roayaie, R. Lencioni, K. Koike, J. Zucman-Rossi and R. S. Finn, *Nat. Rev. Dis. Primers*, 2021, **7**, 6–34.

60 A. Gupta, R. Sedhom and M. S. Beg, *JAMA Oncol.*, 2020, **6**, 308.

61 Y. Liu, L. Teng, C. Xu, T.-B. Ren, S. Xu, X. Lou, L. Yuan and X.-B. Zhang, *CCS Chem.*, 2022, **4**, 2153–2164.

62 X. Liu, B. Yu, Y. Shen and H. Cong, *Coord. Chem. Rev.*, 2022, **468**, 214609–214642.

63 S. Liu, C. Chen, Y. Li, H. Zhang, J. Liu, R. Wang, S. T. H. Wong, J. W. Y. Lam, D. Ding and B. Z. Tang, *Adv. Funct. Mater.*, 2019, **30**, 1908125–1908134.